CHINESE OPTICS LETTERS

Vol. 19, No. 2 | February 2021

Doublet achromatic metalens for broadband optical retroreflector

Ming Deng (邓 明), Tangxuan Ren (任唐轩), Jian Wang (王 健), and Lin Chen (陈 林)*

Wuhan National Laboratory for Optoelectronics, Huazhong University of Science and Technology, Wuhan 430074, China

*Corresponding author: chen.lin@mail.hust.edu.cn

Received July 24, 2020 | Accepted September 11, 2020 | Posted Online January 11, 2021

A retroreflector that reflects light along its incident direction has found numerous applications in photonics, but the available metasurface schemes suffer from the issue of narrow bandwidth and/or a single angle of incidence. Here, a retroreflector using double layers of achromatic gradient metasurfaces is reported, which can realize retroreflection over a continuous range of incidence angles within a wide spectral band. The first metasurface serves as a transmissive achromatic lens that performs a broadband spatial Fourier transform and its inverse, while the second metasurface works as a reflective achromatic lens that undergoes wavelength- and position-dependent phase dispersions. Using this design strategy, a near-infrared retroreflector comprised of silicon nanopillars with the cross sections of square pillars and square holes is numerically demonstrated, providing a high-performance retroreflection for polarization-independent incident light waves over a continuous range of incidence angles from 0° to 16° within an extremely broad wavelength range between 1.35 and 1.95 μm. The scheme herein can offer a design strategy of broadband retroreflectors and impact numerous photonics applications.

Keywords: metasurfaces; retroreflectors; broadband; polarization independence.

DOI: 10.3788/COL202119.023601

1. Introduction

Metasurfaces, artifically designed ultrathin two-dimensional (2D) materials composed of subwavelength resonators, exhibit extraordinary electromagenetic (EM) properties that are unattainable with natural materials. Metasurfaces have shown great potentials to tailor the wavefront of EM waves, which has led to various intriguing effects, such as light bending[1–4], unidirectional surface plasmon coupling[5], invisibility cloaks[6], flat lenses[7–9], holography[10–12], and generation of vortex beams[1,13–15]. Optical retroreflectors capable of reflecting the incoming light wave along its incident direction are very important components in communications[16,17], remote sensing[18], and laser tracking[19]. Conventional retroreflectors rely on the utilization of macroscopic geometrical structures, such as a corner-cube retroreflector[20] and Eaton lens[21,22], are bulky and nonplanar and, hence, inconveniently compatible for intergration and miniaturization. Metasurfaces have recently shown great promise for building flat ultrathin retroreflectors that demonstrate its superiority over conventional schemes in terms of compactness and intergration.

Initially, plasmonic metasurfaces/metagratings have been used to realize retroreflection, but the resultant experiment exhibits limited working bandwidth and/or a single incidence angle since the provided tangential momenta are fixed after the fabrication process[23–26]. To address the issue of limited working incidence angle, reconfigurable plasmonic metasurfaces/metagratings have been proposed and demonstrated, which realizes spin-polarized retroreflection with a discrete/continuous angle of incidence at a single frequency[27,28]. Analogous to conventional cat's eye retroreflectors[19,29], it has been proposed to employ cascaded gradient metasurfaces[30]. This scheme has shown the capability of retroreflecting light over a continuous angle at a single frequency. However, all of the aforementioned schemes undergo narrow bandwidth, which limits practical applications, as the device bandwidth is crucial for an optical system. To date, realizing an optical metasurface retroreflector with a broad operation bandwidth, continuous incidence angles, and polarization independence remains largely unexplored. Here, a broadband retroreflector with a continuous range of incidence angles is proposed by the use of two layers of achromatic gradient metasurfaces. The first metasurface serves as a transmissive achromatic lens that performs a broadband spatial Fourier transform and its inverse, while the second metasurface works as a reflective achromatic lens that undergoes wavelength- and position-dependent phase dispersions. We numerically demonstrate a near-infrared retroreflector that provides a high-performance retroreflection for

polarization-independent incident light waves over a continuous range of incidence angles within an extremely broad wavelength range.

2. Results and Discussions

2.1. Design principle

The transmissive achromatic gradient metasurface is schematically shown in Fig. 1(a), which enables a light source with a continuously changing wavelength to share the same focal length over a wide continuous range of incidence angles [Figs. 1(b) and 1(c)]. The required phase distributions of $\varphi^L(r_0,\lambda)$ for an achromatic metalens should abide by[31,32]

$$\varphi^L(r_0,\lambda)-\varphi^L(0,\lambda)=-n\frac{2\pi}{\lambda}\left(\sqrt{F^2+r_0^2}-F\right), \tag{1}$$

where $r_0=\sqrt{x^2+y^2}$ is the distance between an arbitrary position and the center of the metalens, n is the refractive index of the medium below the metalens, and λ is the wavelength in free space. Figure 1(j) schematically depicts the required spectral phase profiles for the central meta-unit and spatial phase profiles

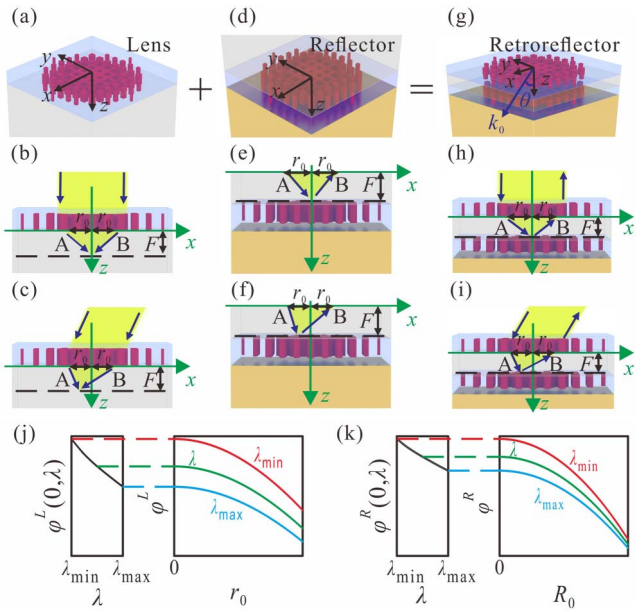

Fig. 1. (a)–(c) Schematic of (a) a transmissive achromatic metasurface that enables a light source with a continuously changing wavelength to have (b), (c) the same focal point. (d)–(f) Schematic of (d) a reflective achromatic metasurface that bestows a twice tangential momentum to (e), (f) the incoming light source with continuously changed wavelength. (g)–(i) Schematic of a broadband retroreflector comprised of a transmissive achromatic metasurface combined with a reflective achromatic metasurface. (j), (k) Spectral phase profiles (left panel) for the central meta-unit and spatial phase profiles (right panel) along the radial direction for a (j) transmissive/(k) reflective achromatic metalens within an arbitrary wavelength range of $\lambda\in[\lambda_{min},\lambda_{max}]$.

along the radial direction. Once light waves with an incidence angle of θ ($0°\le\theta<90°$) illuminating the metalens are focused at the focal plane, the foci offset $l(\theta)$ is proportional to $\sin\theta$[33]:

$$\sin\theta=nl(\theta)/F, \tag{2}$$

provided that $r_0^2, l(\theta)^2\ll F^2$. The reflective metasurface [Fig. 1(d)] placed at the focal plane should bestow a twice tangential momentum to the incoming light source so that the reflective waves experience retroreflection[30], and the phase distributions of $\varphi^R(R_0,\lambda)$ follow

$$\left.\frac{\partial\varphi^R(R_0,\lambda)}{\partial R_0}\right|_{R_0=l(\theta)}=-2\left(\frac{2\pi}{\lambda}\right)\sin\theta, \tag{3}$$

where $R_0=\sqrt{x^2+y^2}$ is the distance between an arbitrary position and the center of the reflective metasurface. In this case, the reflective light waves reach position B that is symmetrical to position A with respect to the optical axis of the transmissive metalens [Figs. 1(e) and 1(f)]. $\varphi^R(R_0,\lambda)$ can be derived by incorporating Eq. (2) into Eq. (3):

$$\varphi^R(R_0,\lambda)-\varphi^R(0,\lambda)=-\frac{2\pi}{\lambda}\frac{n}{F}R_0^2. \tag{4}$$

Equation (4) indicates that the required reflective metasurface is an achromatic metalens as well and has a focal length of $F/2$[29]. Figure 1(k) schematically depicts the required spectral phase profiles for the center meta-unit and spatial phase profiles along the radial direction for the achromatic metalens. A broadband retroreflector can thus be built with a combination of the transmissive and the reflective achromatic metalenses [Fig. 1(g)]. An incident light is anticipated to be reflected back to its incident direction over a continuous range of incidence angles, regardless of its wavelength [Figs. 1(h) and 1(i)].

2.2. Design and demonstration of broadband metasurface retroreflector

We introduce silicon metasurfaces with square pillars and square holes[31], as shown in Figs. 2(a) and 2(b), to provide diverse phase dispersions required to construct achromatic metalens. We firstly select the geometrical parameters for the center meta-unit of the transmissive (reflective) metalens with the phase of $\varphi^L(0,\lambda)$ [$\varphi^R(0,\lambda)$]. Afterwards, the meta-unit at an arbitrary radius [r_0 (R_0) for the transmissive (reflective) metalens] can be selected out if its phase profile is mostly close to the distributions extracted by Eqs. (1) and (4). The optimized meta-units at r_0 (R_0) are selected out by use of the method of mean square error. Considering that there are multiple discrete wavelengths λ_i ($i=1,2,\ldots,N$) within the wavelength range $[\lambda_{min},\lambda_{max}]$ and M meta-units for the transmissive (reflective) achromatic metalens, the mean square error is retrieved as $\frac{1}{N}\sum_{i=1}^{N}[\varphi^L_{unit,m}(\lambda_i)-\varphi^L(r_0,\lambda_i)]^2$ ($\frac{1}{N}\sum_{i=1}^{N}[\varphi^R_{unit,m}(\lambda_i)-\varphi^R(R_0,\lambda_i)]^2$) for the transmissive (reflective) achromatic metalens, where $\varphi^L_{unit,m}(\lambda)$ [$\varphi^R_{unit,m}(\lambda)$] represents the phase profile of the mth unit

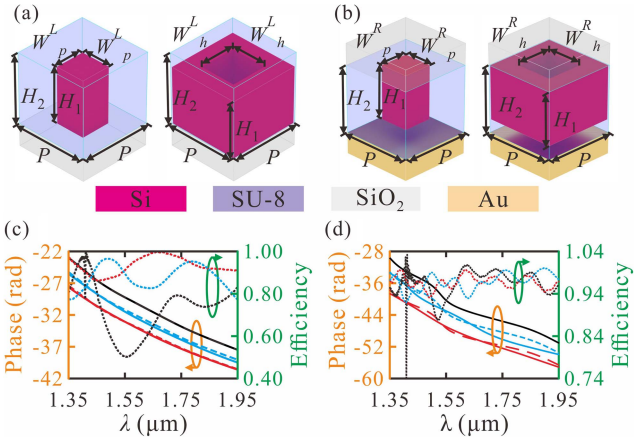

Fig. 2. (a), (b) Schematics of (a) the transmissive meta-units comprised of silicon square pillars and square holes, and (b) the reflective meta-units comprised of silicon square pillars and square holes on a gold film. (c) Theoretical transmission phase profiles for the transmissive metalens at $r_0 = 6.3\,\mu$m (red dashed line), 4.5 μm (azure dashed line), and 0 (black dashed line), associated with the simulated transmission efficiencies (red, azure, and black dotted lines) and phase profiles (red, azure, and black solid lines) of three meta-units with $W_p^L = 0.18\,\mu$m, $W_h^L = 0.34\,\mu$m, and $W_h^L = 0.10\,\mu$m, respectively. (d) Theoretical reflection phase profiles for the reflective metalens at $R_0 = 5.4\,\mu$m (red dashed line), 3.6 μm (azure dashed line), and 0 (black dashed line), associated with the simulated reflection efficiencies (red, azure, and black dotted lines) and phase profiles (red, azure, and black solid lines) of three meta-units with $W_p^R = 0.20\,\mu$m, $W_h^R = 0.32\,\mu$m, and $W_h^R = 0.18\,\mu$m, respectively. The lattice constants along the x and y directions are $P = 0.45\,\mu$m, and the thickness of silicon is $H_1 = 0.6\,\mu$m. The silicon layer is covered by SU-8 polymer, with the thickness and refractive index being $H_2 = 2\,\mu$m and 1.555, respectively, and the refractive indices of other materials are extracted from Ref. [34].

among all of the units. The meta-unit at r_0 (R_0) selected out as the mean square error is minimum.

Figures 2(c) and 2(d) show the transmission/reflection efficiencies and phase profiles of three transmissive/reflective meta-units, where the simulated phase agrees well with the theoretical value predicted by Eqs. (1) and (4). The numerical simulations are conducted by the finite-difference time-domain (FDTD) method with the commercial software Lumerical FDTD Solutions. It should be emphasized here that the used meta-units have four-fold symmetry that enables them to work with polarization independence. By arranging the meta-units along the x/y directions to follow the achromatic phase profiles in Figs. 1(j) and 1(k), a broadband achromatic transmissive/reflective metalens with a continuous range of incidence angles can be successfully designed. Figure 3(a) shows that the achromatic transmissive metalens light waves of 1.35–1.95 μm with 0° and 16° incidence angles can be focused at the predesigned focal plane with a focal length of 22 μm. It should be noted here that light waves with other incidence angles between 0° and 16° within the wavelength range of interest can also be focused at

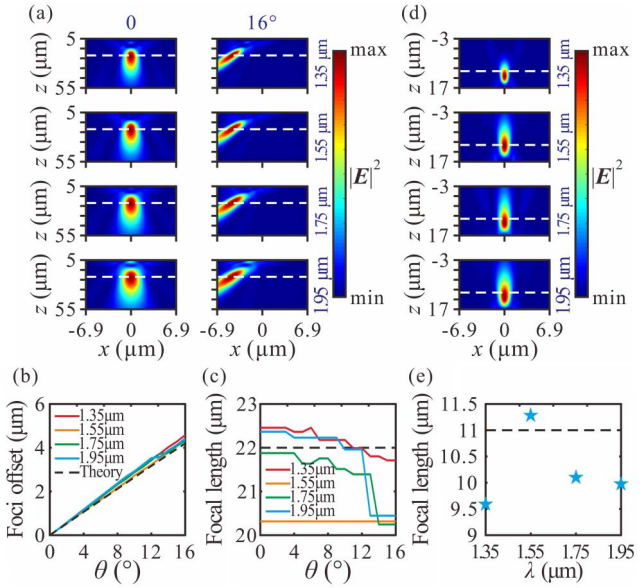

Fig. 3. (a) Distributions of $|E|^2$ in the x–z plane for the transmissive metalens of 13.95 μm in diameter under the illumination of x-polarized light waves with 0° and 16° at 1.35, 1.55, 1.75, and 1.95 μm. (b) Foci offsets and (c) focal lengths versus incidence angle for four wavelengths (1.35, 1.55, 1.75, and 1.95 μm). (d) Distributions of $|E|^2$ in the x–z plane for the reflective metalens of 12.15 μm in diameter under the normal illumination of x-polarized light waves at 1.35, 1.55, 1.75, and 1.95 μm. (e) Focal length of the reflective metalens versus light wavelength.

the same focal plane, which has not been shown here. The simulated foci offsets and focal lengths are all consistent with the theoretically predicted values [Figs. 3(b) and 3(c)]. With the designed focal length of $F/2$ (11 μm) for the bottom reflective achromatic metalens, the simulated distributions of $|E|^2$ at the four wavelengths and the focal length versus wavelength are presented in Figs. 3(d) and 3(e), clearly indicating that all the incident light waves with normal incidence are reflected and focused at the same point. Achromatic reflective focusing performance can be verified using light illumination at an arbitrary wavelength within 1.35–1.95 μm as well.

The broadband metasurface retroreflector can be built by placing the bottom achromatic reflective metalens at the focal plane of the transmissive one (Fig. 1). The dielectric spacer between the transmissive and reflective achromatic metalenses is assumed to be silica with the thickness being equal to F. The electric-field distributions in the far-field region above the metasurface retroreflector can be retrieved by use of the inverse Fourier transform[35]:

$$E_{\mathrm{ref},v}(x,y=0,z,\theta,\lambda) = (2\pi)^{-2}\int\int_{-\infty}^{+\infty} A_v(k_x,k_y,\theta,\lambda)e^{jk_x x - j\sqrt{(2\pi/\lambda)^2-k_x^2-k_y^2}(z-z_0)}\mathrm{d}k_x\mathrm{d}k_y, \tag{5}$$

where $E_{\mathrm{ref},v}(x,y,z,\theta,\lambda)$ denotes the $x\,(y)$ component of the reflected electric field under x-polarized (y-polarized) incidence,

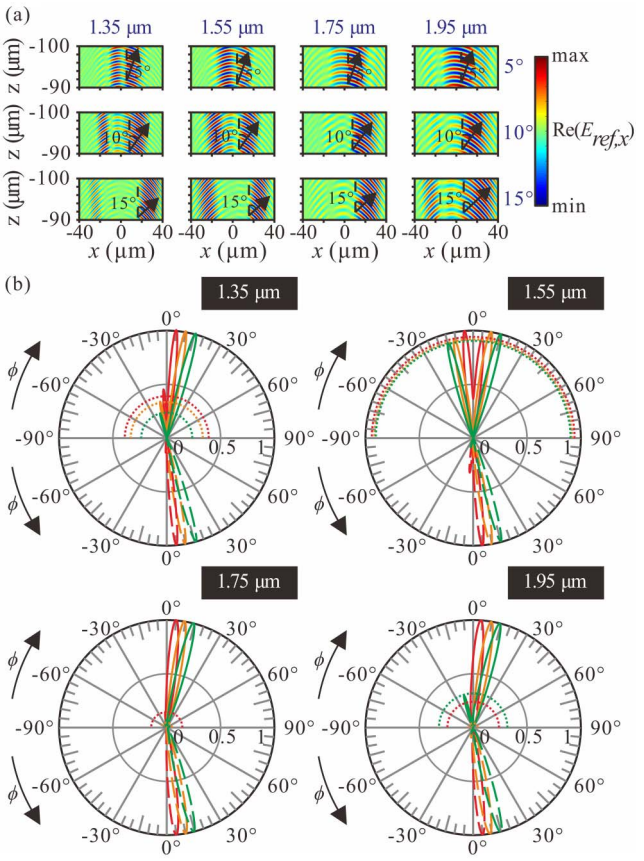

Fig. 4. (a) Distributions of the real part of $E_{\mathrm{ref},x}$ for the broadband metasurface retroreflector under the illumination of *x*-polarized light waves for four wavelengths and three incidence angles (5°, 10°, and 15°). (b) In the upper semicircles, the normalized $|A_x(\varphi,k_y=0,\theta,\lambda)|^2$ (solid lines, with respect to its maximum value) versus spatial angle φ and $\min[|r_{\mathrm{ret}}(\theta,\lambda)|^2,|r_{\mathrm{nor}}(\theta,\lambda)|^2]/\max[|r_{\mathrm{ret}}(\theta,\lambda)|^2,|r_{\mathrm{nor}}(\theta,\lambda)|^2]$ (dotted arcs) under the *x*-polarized incidence for different wavelengths and incidence angles: 5° (red), 10° (orange), and 15° (green). In the lower semicircles, the normalized $|\Delta A_x(\varphi,k_y=0,\theta,\lambda)|^2$ (dashed lines, with respect to its maximum value) versus spatial angle φ for different wavelengths and incidence angles: 5° (red), 10° (orange), and 15° (green).

$A_v(k_x,k_y,\theta,\lambda)=\int\int_{-\infty}^{+\infty}E_{\mathrm{ref},v}(x,y,z=z_0,\theta,\lambda)e^{-jk_xx-jk_yy}\,\mathrm{d}x\mathrm{d}y$, and v stands for $x\,(y)$. z_0 denotes the distance that departs from the retroreflector, and $E_{\mathrm{ref},v}(x,y,z=z_0,\theta,\lambda)$ represents the electric field at the z_0 plane ($z_0=-3.5$ μm in our case). The reflected electric field can be decomposed into an infinite number of plane wave components, and the wavenumber of each component is represented by $\left(k_x,k_y,-\sqrt{(2\pi/\lambda)^2-k_x^2-k_y^2}\right)$. Figure 4(a) presents the distributions of the real part of $E_{\mathrm{ref},x}$ in the far-field region from $z=-90$ μm to -100 μm. It can be clearly seen that light waves of different wavelengths and incidence angles can be reflected back along the incidence directions. The upper semicircles in Fig. 4(b) present the normalized $|A_x(\varphi,k_y=0,\theta,\lambda)|^2$ (with respect to its maximum value) versus the spatial angle φ for different wavelengths and incident angles, where φ is retrieved as $\varphi=\arctan[\lambda k_x/(2\pi)]$ ($|k_x|\le\pi/\lambda$). On one hand, Fig. 4(b) further demonstrates that a portion of the light waves are reflected back along the incidence directions. On the other hand, Fig. 4(b) clearly shows there is also a portion of incident power that emerges on the other side of the normal line of the interface between metasurfaces and air, which is also presented in Fig. 4(a). This branch of reflected light obeys the general Snell's reflection law and is symmetrical to the retroreflected light with respect to the normal line. The ratio between the two main branches of the reflected light in the far-field region is different for different incidence angles or wavelengths. This can be attributed to the fact that the reflectance arising from the transmissive metalens is different for different wavelengths. To remove the reflection of the transmissive metalens, we subtract the reflection field $E^L_{\mathrm{ref},v}(x,y,z,\theta,\lambda)$ of the transmissive metalens from $E_{\mathrm{ref},v}(x,y,z,\theta,\lambda)$, and $\Delta A_v(k_x,k_y,\theta,\lambda)$ is retrieved as

$$\Delta A_v(k_x,k_y,\theta,\lambda)=\int\int_{-\infty}^{+\infty}\Delta E_{\mathrm{ref},v}(x,y,z=z_0,\theta,\lambda)e^{-jk_xx-jk_yy}\mathrm{d}x\mathrm{d}y, \tag{6}$$

with $\Delta E_{\mathrm{ref},v}(x,y,z=z_0,\theta,\lambda)=E_{\mathrm{ref},v}(x,y,z=z_0,\theta,\lambda)-E^L_{\mathrm{ref},v}(x,y,z=z_0,\theta,\lambda)$. The normalized $|\Delta A_x(\varphi,k_y=0,\theta,\lambda)|^2$ (with respect to its maximum value) versus the spatial angle φ for different wavelengths and incident angles is plotted in the lower semicircles in Fig. 4(b). It can be clearly observed that the left branches in the far-field region are highly suppressed. This indicates that the left branches of the reflected light mainly come from the reflection of the transmissive metalens. It is the different reflectance of the transmissive metalens for different incidence angles or wavelengths that results in different ratios between the two main branches of the reflected light.

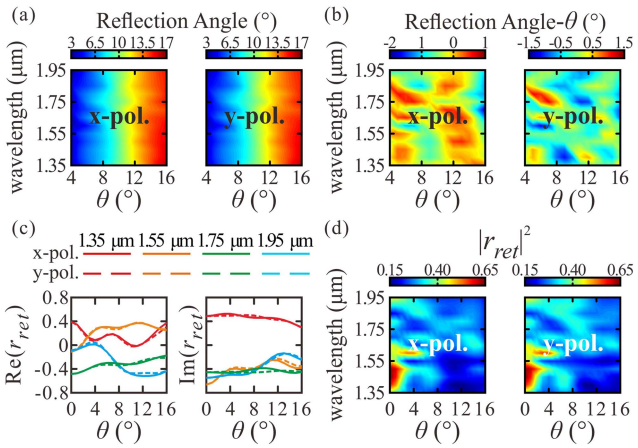

Fig. 5. (a) Reflection angles and (b) the difference between the reflection angles and the incidence angles versus incidence angle and wavelength under *x*- and *y*-polarized incidence. (c) Real and imaginary parts of the retroreflection coefficients $r_{\mathrm{ret}}(\theta,\lambda)$ versus incidence angles under *x*- and *y*-polarized incidence. (d) Values of $|r_{\mathrm{ret}}(\theta,\lambda)|^2$ versus incidence angle and wavelength under *x*- and *y*-polarized incidence.

The reflection angles versus the incidence angle within the wavelength range of interest are presented in Fig. 5(a) and are consistent with the predesigned retroreflection angles. The deviation of the reflection angle and the incidence angle is shown in Fig. 5(b), which clearly indicates that the difference is approximately 1°, almost within the entire wavelength range of interest. A small region merely exists in the left panel of Fig. 5(b), which is associated with the maximum difference of about 1.8° around 1.7 μm under x-polarized incidence of 16°. The slight discrepancy between the simulated angles and the predesigned angles can be attributed to the fact that the phase dispersion of the used transmissive/reflective meta-units does not fully follow the conditions required by Eqs. (1) and (4). It should be noted here, as the reflective metalens has a limited size, there is a restriction for the maximum incidence angle. For an incidence angle of 16°, the focus of the transmissive metalens locates at around the boundary of the reflective metalens. For larger incidence angles, the performance of the broadband metasurface retroreflector will deteriorate, which has not been shown here. An effective method to increase the maximum incidence angle can be realized by use of a transmissive achromatic metalens with a smaller F, which is at the sacrifice of the reduced radii of both metasurfaces.

As the used meta-units have four-fold symmetry and support a waveguide-like cavity resonance mode, the meta-units thus present gentle sensitivity to the polarization states of incidence light, even if the incident direction significantly deviates from the normal line[33]. Therefore, the resultant metasurface retroreflector is highly anticipated to operate with polarization independence. Other cross sectional shapes, such as a circle can also be an alternative for the meta-units. The retroreflection coefficients describing the relation between the incident plane wave component of incidence angle θ and its retroreflective counterpart for x and y polarizations can be estimated as

$$r_{\mathrm{ret}}(\theta,\lambda)=\left[\int\int_{-\infty}^{+\infty}E_{\mathrm{ref},v}(x,y,z=z_0,\theta,\lambda)e^{-\frac{j2\pi}{\lambda}x\sin\theta}\mathrm{d}x\mathrm{d}y\right]\Big/\left[\int\int_{-\infty}^{+\infty}E_{\mathrm{inc},v}(x,y,z=z_1,\theta,\lambda)e^{\frac{j2\pi}{\lambda}x\sin\theta}\mathrm{d}x\mathrm{d}y\right],\quad(7)$$

where $E_{\mathrm{inc},v}(x,y,z,\theta,\lambda)$ denotes the x (y) component of the incident electric field under x-polarized (y-polarized) incidence. z_1 denotes the coordinate along the z axis, in which the incidence source locates, and $E_{\mathrm{inc},v}(x,y,z=z_1,\theta,\lambda)$ represents the electric field of the incidence source. The dependence of the real part and the imaginary part of $r_{\mathrm{ret}}(\theta,\lambda)$ on the incidence angle is shown in Fig. 5(c). It is apparent that $r_{\mathrm{ret}}(\theta,\lambda)$ for x polarization almost coincides with that for y polarization from 0° to 16° incidence angles within the wavelength range of interest. The estimated efficiency of retroreflection, $|r_{\mathrm{ret}}(\theta,\lambda)|^2$, ranges from 0.16 to 0.61 [Fig. 5(d)], lower than that with the grating structures[25–28]. The causes of higher retroreflection efficiency of the grating structures can be attributed to the fact that periodical structures are employed so that the tangential momenta provided by gratings match those of the retroreflected waves. Another coefficient describing the relation between the incident plane wave component of incidence angle θ and its normally reflective counterpart for x and y polarizations can be estimated as

$$r_{\mathrm{nor}}(\theta,\lambda)=\left[\int\int_{-\infty}^{+\infty}E_{\mathrm{ref},v}(x,y,z=z_0,\theta,\lambda)e^{\frac{j2\pi}{\lambda}x\sin\theta}\mathrm{d}x\mathrm{d}y\right]\Big/\left[\int\int_{-\infty}^{+\infty}E_{\mathrm{inc},v}(x,y,z=z_1,\theta,\lambda)e^{\frac{j2\pi}{\lambda}x\sin\theta}\mathrm{d}x\mathrm{d}y\right].\quad(8)$$

The $\min[|r_{\mathrm{ret}}(\theta,\lambda)|^2,|r_{\mathrm{nor}}(\theta,\lambda)|^2]/\max[|r_{\mathrm{ret}}(\theta,\lambda)|^2,|r_{\mathrm{nor}}(\theta,\lambda)|^2]$ under the x-polarized incidence for different wavelengths and incidence angles are plotted in Fig. 4(b) and match well with the ratio between the two branches of the reflected light in the far-field region.

3. Conclusion

In conclusion, we have proposed a strategy of building broadband retroreflectors by use of transmissive and reflective achromatic metalenses. A silicon metasurface retroreflector at the telecom wavelengths is designed and numerically demonstrated by use of this design strategy, demonstrating the capability of retroreflecting polarization-independent light waves with the wavelength range between 1.35 and 1.95 μm over a continuous range of incidence angles from 0° to 16°. The design strategy can also be extended to the visible light band. The presented results point out a promising avenue to design complex metasurface photonic devices that are broadband and polarization friendly.

Acknowledgement

This work was supported by the National Natural Science Foundation of China (Nos. 11674118 and 12074137), the National Major Research and Development Program (No. 2018YFB2200200), and the State Key Laboratory of Advanced Technology for Materials Synthesis and Processing (Wuhan University of Technology).

References

1. N. Yu, P. Genevet, M. A. Kats, F. Aieta, J.-P. Tetienne, F. Capasso, and Z. Gaburro, "Light propagation with phase discontinuities: generalized laws of reflection and refraction," Science **334**, 333 (2011).
2. F. Aieta, M. A. Kats, P. Genevet, and F. Capasso, "Multiwavelength achromatic metasurfaces by dispersive phase compensation," Science **347**, 1342 (2015).
3. X. Yin, H. Zhu, H. Guo, M. Deng, T. Xu, Z. Gong, X. Li, Z. H. Hang, C. Wu, H. Li, S. Chen, L. Zhou, and L. Chen, "Hyperbolic metamaterial devices for wavefront manipulation," Laser Photon. Rev. **13**, 1800081 (2019).
4. Z. Deng, S. Zhang, and G. P. Wang, "Wide-angled off-axis achromatic metasurfaces for visible light," Opt. Express **24**, 23118 (2016).
5. S. Sun, Q. He, S. Xiao, Q. Xu, X. Li, and L. Zhou, "Gradientindex metasurfaces as a bridge linking propagating waves and surface waves," Nat. Mater. **11**, 426 (2012).
6. X. Ni, Z. J. Wong, M. Mrejen, Y. Wang, and X. Zhang, "An ultrathin invisibility skin cloak for visible light," Science **349**, 1310 (2015).

7. X. Chen, L. Huang, H. Mühlenbernd, G. Li, B. Bai, Q. Tan, G. Jin, C. Qiu, S. Zhang, and T. Zentgraf, "Dual-polarity plasmonic metalens for visible light," Nat. Commun. **3**, 1198 (2012).
8. T. Yang, H. Lin, and B. Jia, "Two-dimensional material functional devices enabled by direct laser fabrication," Front. Optoelectron. **11**, 2 (2018).
9. J. Chen, B. Wang, L. Zhu, J. Han, and Q. Xu, "Metalens for coaxial double wavelength focusing," Chin. Opt. Lett. **18**, 042401 (2020).
10. G. Zheng, H. Mühlenbernd, M. Kenney, G. Li, T. Zentgraf, and S. Zhang, "Metasurface holograms reaching 80% efficiency," Nat. Nanotech. **10**, 308 (2015).
11. Z. Deng, J. Deng, X. Zhuang, S. Wang, K. Li, Y. Wang, Y. Chi, X. Ye, J. Xu, G. P. Wang, R. Zhao, X. Wang, Y. Cao, X. Cheng, G. Li, and X. Li, "Diatomic metasurface for vectorial holography," Nano Lett. **18**, 2885 (2018).
12. Z. Deng, J. Deng, X. Zhuang, S. Wang, T. Shi, G. P. Wang, Y. Wang, J. Xu, Y. Cao, X. Wang, X. Cheng, G. Li, and X. Li, "Facile metagrating holograms with broadband and extreme angle tolerance," Light Sci. Appl. **7**, 78 (2018).
13. M. I. Shalaev, J. Sun, A. Tsukernik, A. Pandey, K. Nikolskiy, and N. M. Litchinitser, "High-efficiency all-dielectric metasurfaces for ultracompact beam manipulation in transmission mode," Nano Lett. **15**, 6261 (2015).
14. L. Zhu and J. Wang, "A review of multiple optical vortices generation: methods and applications," Front. Optoelectron. **12**, 52 (2019).
15. C. Wan, G. Rui, J. Chen, and Q. Zhan, "Detection of photonic orbital angular momentum with micro- and nano-optical structures," Front. Optoelectron. **12**, 88 (2019).
16. P. Villoresi, T. Jennewein, F. Tamburini, M. Aspelmeyer, C. Bonato, R. Ursin, C. Pernechele, V. Luceri, G. Bianco, A. Zeilinger, and C. Barbieri, "Experimental verification of the feasibility of a quantum channel between space and Earth," New J. Phys. **10**, 033038 (2008).
17. G. C. Gilbreath, W. S. Rabinovich, T. J. Meehan, M. J. Vilcheck, R. Mahon, R. Burris, M. Ferraro, I. Solkolsky, J. A. Vasquez, C. S. Bovais, K. Cochrell, K. C. Goins, R. Barbehenn, D. S. Katzer, K. Ikossi-Anastasiou, and M. J. Montes, "Large-aperture multiple quantum well modulating retroreflector for free-space optical data transfer on unmanned aerial vehicles," Opt. Eng. **40**, 1348 (2001).
18. D. D. Nelson, M. S. Zahniser, J. B. McManus, C. E. Kolb, and J. L. Jimenez, "A tunable diode laser system for the remote sensing of on-road vehicle emissions," Appl. Phys. B **67**, 433 (1998).
19. T. Takatsuji, M. Goto, S. Osawa, R. Yin, and T. Kurosawa, "Whole-viewing-angle cat's-eye retroreflector as a target of laser trackers," Meas. Sci. Technol. **10**, N87 (1999).
20. L. Zhou, J. M. Kahn, and K. S. J. Pister, "Corner-cube retroreflectors based on structure-assisted assembly for free-space optical communication," J. Microelectromech. Syst. **12**, 233 (2003).
21. M. R. Forouzeshfard and T. Tyc, "Photonic crystals composed of Eaton lenses and invisible lenses," Phys. Rev. A **95**, 013822 (2017).
22. Y. G. Ma, C. K. Ong, T. Tyc, and U. Leonhardt, "An omnidirectional retroreflector based on the transmutation of dielectric singularities," Nat. Mater. **8**, 639 (2009).
23. Y. Jia, J. Wang, Y. Li, Y. Pang, J. Yang, Y. Fan, and S. Qu, "Retro-reflective metasurfaces for backscattering enhancement under oblique incidence," AIP Adv. **7**, 105315 (2017).
24. Y. Jia, J. Wang, J. Yang, Y. Li, Y. Pang, Y. Fan, S. Sui, and S. Qu, "Wideband planar retro-reflective metasurfaces for backscattering enhancement under oblique incidence," J. Phys. D **51**, 335103 (2018).
25. A. M. H. Wong, P. Christian, and G. V. Eleftheriades, "Binary Huygens' metasurfaces: experimental demonstration of simple and efficient near-grazing retroreflectors for TE and TM polarizations," IEEE Trans. Antennas Propag. **66**, 2892 (2018).
26. V. S. Asadchy, A. Díaz-Rubio, S. N. Tcvetkova, D. H. Kwon, A. Elsakka, M. Albooyeh, and S. A. Tretyakov, "Flat engineered multichannel reflectors," Phys. Rev. X **7**, 031046 (2017).
27. L. Yan, W. Zhu, M. F. Karim, H. Cai, A. Y. Gu, Z. Shen, P. H. J. Chong, D. Kwong, C. Qiu, and A. Q. Liu, "$0.2\lambda_0$ thick adaptive retroreflector made of spin-locked metasurface," Adv. Mater. **30**, 1802721 (2018).
28. M. Li, L. Jing, X. Lin, S. Xu, L. Shen, B. Zheng, Z. Wang, and H. Chen, "Angular-adaptive spin-locked retroreflector based on reconfigurable magnetic metagrating," Adv. Opt. Mater. **7**, 1900151 (2019).
29. J. J. Snyder, "Paraxial ray analysis of a cat's-eye retroreflector," Appl. Opt. **14**, 1825 (1975).
30. A. Arbabi, E. Arbabi, Y. Horie, S. M. Kamali, and A. Faraon, "Planar metasurface retroreflector," Nat. Photon. **11**, 415 (2017).
31. S. Wang, P. C. Wu, V. Su, Y. Lai, M. Chen, H. Y. Kuo, B. H. Chen, Y. H. Chen, T. Huang, J. Wang, R. Lin, C. Kuan, T. Li, Z. Wang, S. Zhu, and D. P. Tsai, "A broadband achromatic metalens in the visible," Nat. Nanotech. **13**, 227 (2018).
32. L. Li, Q. Yuan, R. Chen, X. Zou, W. Zang, T. Li, G. Zheng, S. Wang, Z. Wang, and S. Zhu, "Chromatic dispersion manipulation based on metasurface devices in the mid-infrared region," Chin. Opt. Lett. **18**, 082401 (2020).
33. W. Liu, Z. Li, H. Cheng, C. Tang, J. Li, S. Zhang, S. Chen, and J. Tian, "Metasurface enabled wide-angle fourier lens," Adv. Mater. **30**, 1706368 (2018).
34. E. D. Palik, *Handbook of Optical Constants of Solids* (Academic, 1989).
35. T. Paul, C. Rockstuhl, C. Menzel, and F. Lederer, "Anomalous refraction, diffraction, and imaging in metamaterials," Phys. Rev. B **79**, 115430 (2009).